ARTICLE

Check for updates

Arctic cyclones have become more intense and longer-lived over the past seven decades

Xiangdong Zhang [1✉], Han Tang[2], Jing Zhang[3], John E. Walsh[2], Erika L. Roesler[4], Benjamin Hillman[4], Thomas J. Ballinger [2] & Wilbert Weijer [5]

Intense cyclones driving extreme Arctic weather and climate events have been more frequently observed during recent years, causing dramatic environmental and socioeconomic impacts. However, inconsistencies have emerged about long-term changes in Arctic cyclone activity. Here we analyze multiple reanalysis datasets covering a multidecadal period with improvements to the cyclone tracking algorithm and the integrated cyclone activity metric. The results indicate an intensification of Arctic cyclone activity over the last seven decades. There has been a long-term shift of the maximum cyclone counts from weaker to stronger cyclones and a pronounced lengthening of the duration of strong cyclones. Spatial analysis shows increased strong cyclone frequency over the Arctic, driven by enhanced lower troposphere baroclinicity, amplified winter jet stream waves over the subpolar North Atlantic, and a strengthened summer tropospheric vortex over the central Arctic. The stratospheric vortex has also intensified the tropospheric waves and vortex with distinct dynamics between winter and summer. Recently enhanced baroclinicity over large areas of the Arctic and midlatitudes suggests more complicated atmospheric dynamics than what is hypothesized with Arctic-amplification-induced decrease in meridional temperature gradients.

[1] North Carolina State University, Asheville, NC 28801, USA. [2] University of Alaska Fairbanks, Fairbanks, AK 99775, USA. [3] North Carolina A&T State University, Greensboro, NC 27411, USA. [4] Sandia National Laboratories, Albuquerque, NM 87185, USA. [5] Los Alamos National Laboratory, Los Alamos, NM 87545, USA. ✉email: xzhan238@ncsu.edu

Arctic cyclones are a fundamental component of atmospheric circulation, with variability over a range of timescales. They can originate in the midlatitudes or be generated within the Arctic[1–4]. Cyclones that originate in the midlatitudes and subarctic play important roles in linking the Arctic climate to the lower latitudes by driving poleward transient heat and moisture transport[5–9]. Arctic cyclones can greatly change air temperature, humidity, and winds; form clouds; cause rainfall and snowfall; and then modulate surface turbulent and radiative fluxes. Accordingly, they may enhance atmosphere-sea ice-ocean interactions and cumulatively contribute to large-scale variability and long-term changes in the Arctic climate[2,10–13].

In particular, strong cyclones (e.g., the cyclones in the summers of 2012 and 2016 and the winter of 2022 with central sea level pressures (SLPs) deeper than 970 hPa) have been reported in the Arctic during recent decades[14–18]. Associated with the strong cyclones, weather and climate extremes have been observed, including rapid sea ice loss, winter heat waves, atmospheric rivers, heavy precipitations, strong winds, coastal flooding, rain-on-snow/ice events, and Greenland Ice Sheet melt[7,18–26]. Not only do these extreme events have dramatic environmental and socioeconomical impacts, but they may also reduce the resilience of the Arctic climate system by accelerating its long-term changes in a nonlinear manner. Therefore, it is imperative to improve understanding of the changing characteristics of Arctic cyclone activity and to investigate the underlying physical mechanisms.

Earlier studies have suggested the intensification of Arctic cyclone activity based on SLP data[2], which was supported by the use of the upper air relative vorticity[5]. However, inconsistencies and vigorous debates about long-term changes in Arctic cyclone activity have emerged across recent studies using reanalysis datasets. Results from these studies show sensitivities to the parameters describing cyclone activity, the algorithm employed, the datasets used, and the periods selected[11,27–32]. These inconsistencies and debates are even more pronounced in model simulations for historical time periods and projections under future global warming scenarios[33–36].

To reconcile the inconsistencies and discrepancies mentioned above for detecting robust signals of Arctic cyclone changes, we provide an integrated assessment of Arctic cyclone activity using multiple reanalysis datasets covering more than seven decades (see "Methods"), substantially extending the time periods used in previous studies. In the present analysis, we employ an improved cyclone identification and tracking algorithm and an improved integrative cyclone activity metric. We also investigate the underlying physical processes and mechanisms. While possible data biases may cause uncertainties in the identification of the changes in Arctic cyclone activity, the robustness of the results can be enhanced if they are supported by solid physical mechanisms. Accordingly, we synthesize information on the physical and dynamical processes associated with the changes in Arctic cyclone activity. The findings here also provide benchmarks for evaluating model simulations and future projections of Arctic cyclone activity.

Results

Intensification of Arctic cyclone activity. We applied an improved cyclone identification and tracking algorithm (see "Methods") to the three reanalysis datasets and created corresponding cyclone databases, including cyclogenesis and cyclolysis times, cyclone location, cyclone central SLP, and mean SLP gradient within the defined radius of each cyclone center at each time step. We then derived cyclone tracks and calculated monthly energy-based cyclone activity index (EnCAI; see "Methods") based on the cyclones propagating into or being generated within the Arctic (north of 60°N). The Arctic EnCAIs demonstrate large monthly-to-decadal variability from January 1950 (1958 for JRA-55) through December 2021 (Fig. 1). The three reanalysis datasets show strong agreement, in particular in phase transitions, though there are small differences in amplitude. This suggests that all three reanalysis datasets consistently capture the variability of Arctic cyclone activity as measured by EnCAI. The consistency can be attributed to two factors: (1) the cyclones in the Arctic are an integrated element of the large-scale atmospheric circulation, as shown in the following sections of this study. Therefore, the model-data assimilation systems for generating the reanalysis datasets, which are largely constrained by SLP observations outside the data-sparse Arctic, are able to replicate the large-scale atmospheric circulation patterns and capture the realistic cyclone development in the Arctic; and (2) the SLP observations within the Arctic, though limited (such as those by drifting ice stations back to the mid-19th century), provided further constraints locally.

An additional potential concern is the influence of satellite observations, which became available around 1980 and have been assimilated into the reanalysis datasets since then, on the EnCAI time series and trends. However, the three EnCAI time series do not show discontinuities or unusual variations around 1980. Instead, their fluctuations around 1980 are well within the range of one standard deviation of its long-term variability. Moreover, while the three reanalysis datasets assimilated different amounts of satellite observations with different approaches, there are no identifiable systematic errors in the EnCAIs between the three reanalysis datasets. The aggregation of the evidence suggests that
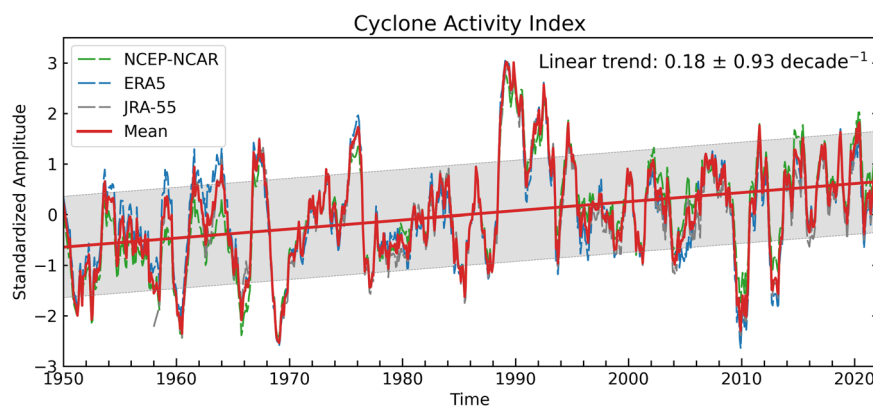

Fig. 1 Arctic cyclone activity index. The standardized energy-based cyclone activity index (EnCAI) for the Arctic (north of 60°N) from January 1950 to December 2021 for the NCEP-NCAR (green curve), ERA5 (blue curve), and JRA-55 (gray curve) datasets. The red curve shows the multi-dataset mean EnCAI. The red straight line is a linear trend of the mean EnCAI. The gray shading indicates ±1.0 the standard deviation relative to the linear trend.

there is a minimum influence of the transition to satellite data assimilation on long-term EnCAI. This conclusion is supported by the two factors discussed above and by the physical processes analysis below.

To simplify the analysis and enhance the robustness of the results, we averaged the three EnCAI time series in the following analysis (the red curve in Fig. 1; simply denoted as EnCAI below). The EnCAI amplitude varies largely with time. A remarkable phenomenon is its anomalously positive polarity from the late 1980s to the early 1990s, indicating the intensification of Arctic cyclone activity. This variation coincides with a similarly prolonged anomaly in the Arctic Oscillation (AO; Supplementary Fig. S1)[37], which was noted in our previous cyclone study[2]. The coincidence can be attributed to the two-way interactive processes between the synoptic and large-scale atmospheric circulation dynamics. Daily resolved synoptic cyclones are an integral part of the large-scale atmospheric circulation. They cumulatively contribute to the monthly mean state of SLP, whose major variability is represented by the AO. On the other hand, the large-scale atmospheric circulation associated with the AO, especially the corresponding upper-level jet streams, drives cyclone developments and steers cyclone propagations. As a consequence, the consistent phenomena occur at both synoptic and large scales. By contrast, following its positive phase into the mid-1990s, the EnCAI amplitude was substantially suppressed following the positive polarity until the mid-2000s. This change also agrees with the neutral phase of the AO during the same period[38,39]. Afterward, the EnCAI amplitude increases to levels generally comparable to or exceeding those of the 1950s to the mid-1990s, including the extremely negative AO/NAO in winter 2010[40].

Superimposed on the large variability, EnCAI has also exhibited a long-term upward trend of 0.18 ± 0.93 (standardized, dimensionless; the second value indicates one standard deviation of variability relative to the trend line) per decade, equal to an increased potential and kinetic energy of 100.78 Joule per unit airmass per decade. The trend is statistically significant at a confidence level of 99% based on a t-test, in which red noise and effective sample size have been taken into account[41]. This long-term trend indicates an intensification of Arctic cyclone activity over the last seven decades (Fig. 1). One question is how the anomalously positive polarity of the EnCAI from the late 1980s to the early 1990s influences the long-term trend. We therefore examined the trends from 1950 to 1988 and from 1996 to 2021, excluding the period of the EnCAI spike. The results show increasing trends of 0.16 ± 0.83 and 0.30 ± 0.78 per decade, respectively. The trend during the recent period is nearly double that during the earlier period. This suggests that the spike does not impact the long-term trend.

The new finding here extends and enhances the robustness of the previous results for an earlier time period of 1948–2002 that was based solely on the NCEP-NCAR reanalysis[2], and it also helps reconcile the recent debates about Arctic cyclone trends[11,27–32]. The trend obtained here is equivalent to a deepening of the Arctic regional mean cyclone central SLP at a rate of 1.20 hPa per decade and an increase in the mean cyclone geostrophic windspeed at a rate of 0.44 m/s per decade. These results suggest that the Arctic regional mean cyclone central SLP and the associated mean geostrophic windspeed have decreased and increased by about 8.64 hPa and 3.20 m/s, respectively, since the 1950s. Note that the EnCAI change rate covers all months. In view of the large climatological annual cycle of sea ice extent, with a minimum in September and a maximum in March, we calculated the EnCAI for these two months. The EnCAI trend is larger in September than in March (Supplementary Fig. S2). This is similar to the long-term sea ice declining trends in these two months. In addition, the EnCAI represents anomalies from the

climatological annual cycle of Arctic cyclone activity with different cyclone counts, intensities, and durations in different months. So, the actual changes in the regional mean cyclone central SLPs and geostrophic windspeeds vary by calendar month. Detailed seasonality analysis will be a follow-up study.

The EnCAI represents an integrated feature of Arctic cyclone activity. To disentangle this feature and better understand the changes in the EnCAI, we examined the time evolution of cyclone counts and durations as a function of cyclone intensity using the combined cyclone datasets from the three reanalysis products. We simply used the cyclone central SLP to represent the intensity and categorized all cyclones into fifteen bins with a bin width of 5.0 hPa for winter (October–March) and summer (April–September) separately. The most prominent feature, superimposed on the low-frequency variability, is a long-term shift of the maximum values of the cyclone count from weaker cyclone categories to stronger cyclone categories in both winter and summer (Fig. 2a, c). A pronounced large increase in strong cyclone count occurred around the mid-1980s, indicating more numerous strong cyclones in the Arctic since that time. We also found notable seasonal differences in the change of cyclone intensity. Winter mean cyclone central SLP has reached 950 hPa or deeper during recent decades. Although summer cyclones have also become stronger, their mean central SLPs have still been much shallower than winter cyclones, generally higher than 960 hPa.

Arctic cyclones have also exhibited an obvious change of prolonged duration (unit: hours) through time (Fig. 2b, d). Unlike the long-term shift of the cyclone count, the duration has shown a general increase for all cyclones across different intensities. The largest duration increase still mainly occurs for the strong cyclones with the central SLP deeper than 980 hPa during winter and ranging from 990 to 960 hPa during summer. When examining the time evolution of strong cyclone duration, we also found a pronounced large increase during the 1980s, consistent with the largest changes in the strong cyclone count around the same time. This suggests that the increased count of strong cyclones has likely been a contributing factor to the increased duration since the 1980s. Moreover, decadal variability, as revealed in our previous study[2], might have also contributed to the remarkable changes in both cyclone count and duration around the mid-1980s.

From the analysis above, Arctic cyclone activity has intensified over the last seven decades, in association with both increased count and prolonged duration of strong cyclones entering or generated within the Arctic. Many previous studies used either cyclone count or duration as an indicator of Arctic cyclone activity. These studies also did not consider the different temporal variations of these metrics for different cyclone intensities. The less integrated nature of these metrics could be the reason for inconsistencies across different trend evaluations. A recent study, for example, shows that cyclone distribution statistics can be quite sensitive to the choice of the metric used for analyzing intensity[32].

Spatial structures of poleward shifted cyclone activity. Given an increase in both count and durations of strong cyclones, a scientific question emerges: Where have the strong cyclones occurred in the Arctic? To address this question, we analyze changes in the spatial distribution of the frequency (or the density; count per $10^5 \, km^2$) of strong cyclone occurrences. To do this, based on the analyses above and Fig. 2 that shows a notable increase in the counts and durations of the cyclones deeper than 990 hPa around the mid-1980s, we (1) define the strong cyclones as those with the central SLP averaged throughout their duration deeper than 990 hPa after either propagating into or being
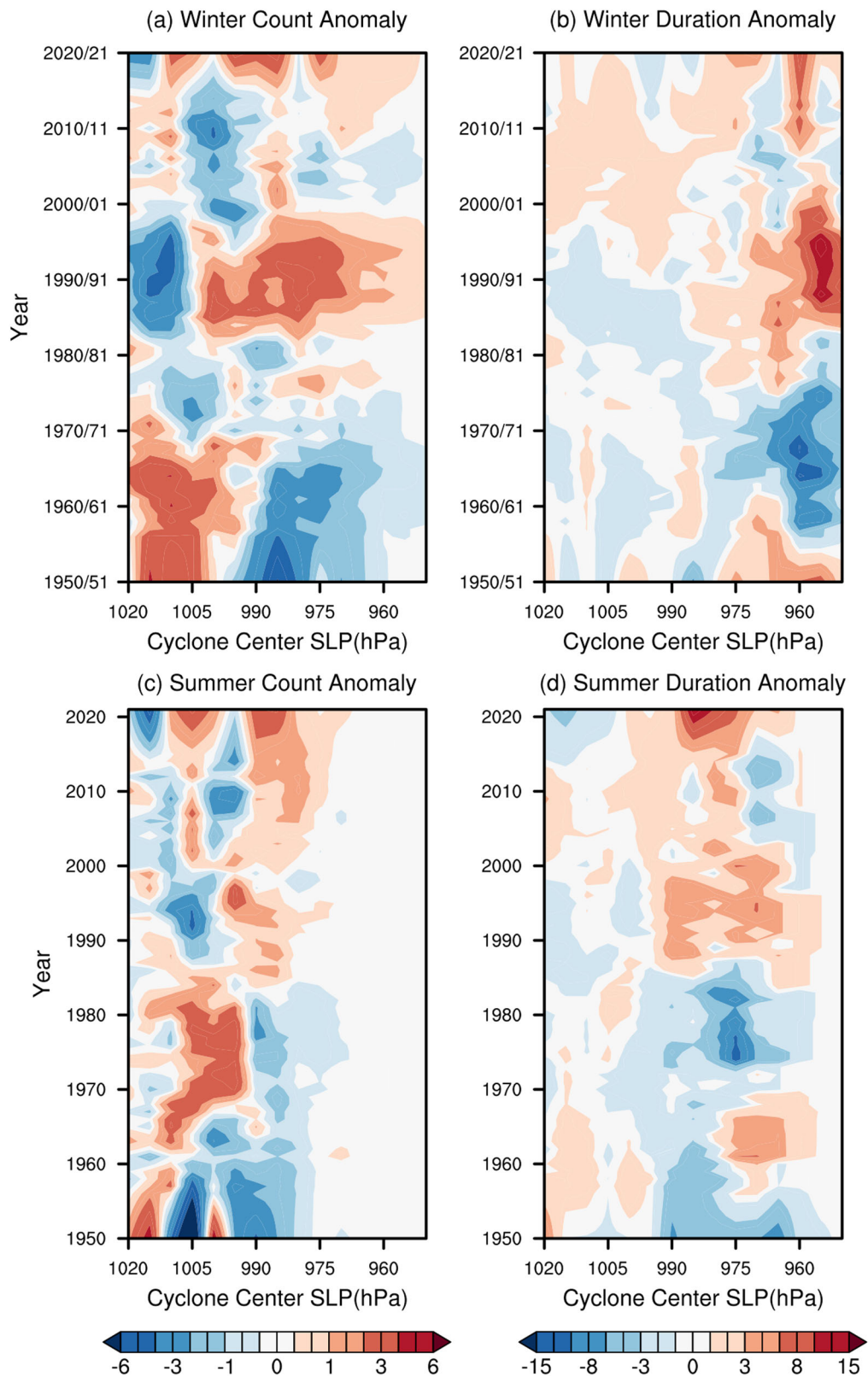
Fig. 2 Time evolution of Arctic cyclone count and duration anomalies. a The count and **b** duration anomalies (unit: hours) of the cyclones that propagate into and are generated within the Arctic region during winter. **c** and **d** are the same as (**a**) and (**b**), but for summer. The anomalies were calculated relative to the corresponding climatological values from 1980 to 2009. (**c**) shows that there are not many summer cyclones deeper than 975 hPa.

generated within the Arctic; and (2) chose two multidecadal periods from 1950/51 to 1984/85 and 1985/86 to 2020/21 for winter and 1950–1985 and 1986–2021 for summer, respectively. We defined a universal spatial resolution at 6.0° × 6.0° to calculate

multidecadal climatological mean frequencies for these two periods using the combined cyclone databases from the three reanalysis datasets. This resolution covers all three different resolutions of the reanalysis datasets and assures a large enough
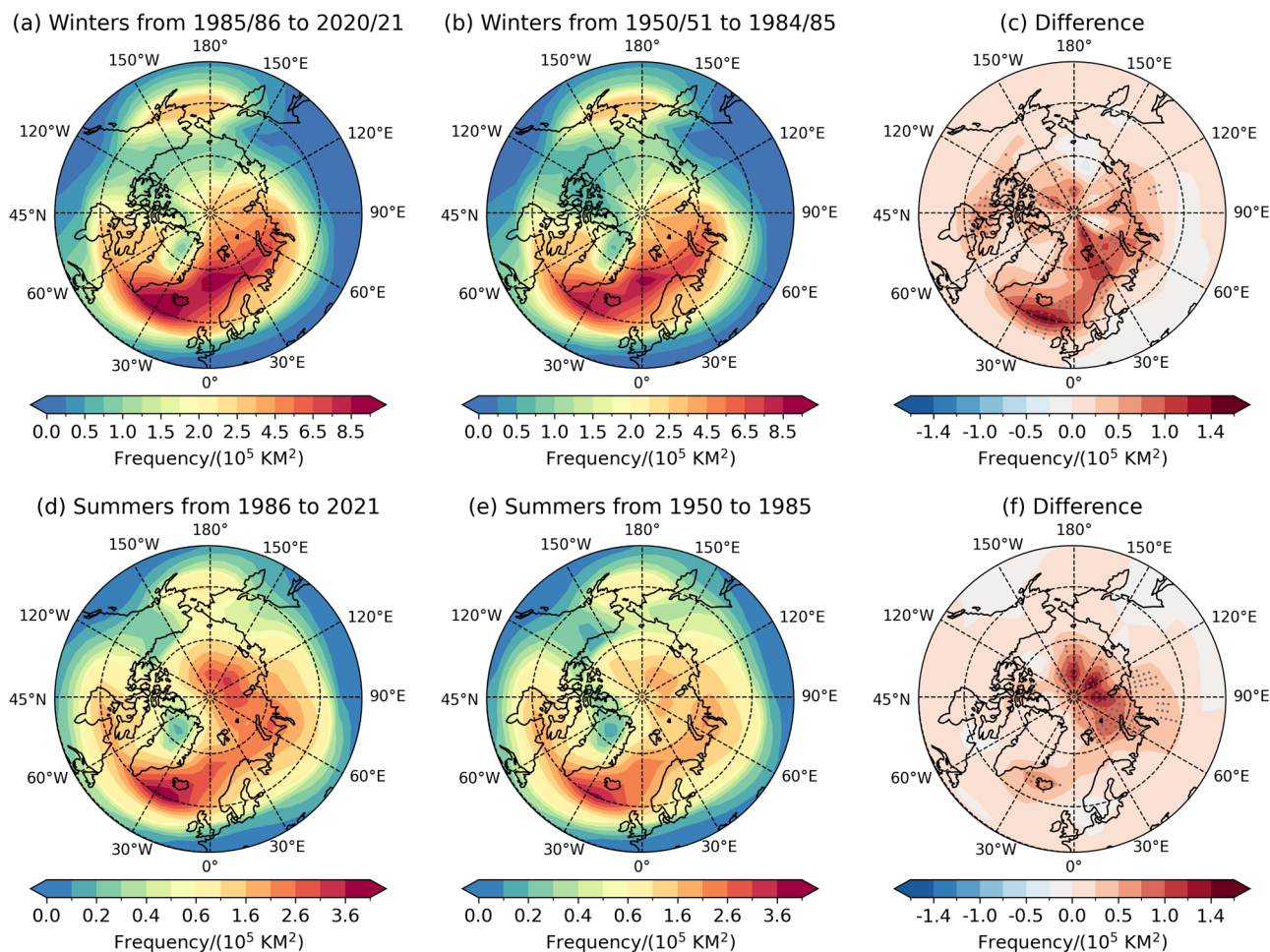
Fig. 3 Spatial structure of Arctic cyclone frequency. Frequency of occurrence of strong cyclones that propagate into or are generated locally within the Arctic region (north of 60°N) for the winters from **a** 1985/86 to 2020/21 and **b** 1950/51 to 1984/85. **c** shows the differences between (**a**) and (**b**). **d–f** are the same as (**a–c**) but for the summers from 1986 to 2021 and from 1950 to 1985. The dots in (**d**) and (**f**) indicate that the differences are statistically significant at the level of $p < 0.10$ using the two-sided t-test.

sample size of strong cyclone occurrence in each grid cell without a loss of essential spatial structures of the cyclone frequency.

The results show a high frequency over the Hudson Bay, Labrador Sea, subpolar North Atlantic, and North Atlantic Arctic during winter for both multidecadal time periods (Fig. 3a, b). A maximum frequency is found over the Irminger Sea, Iceland Basin, and the western Norwegian Sea. The spatial distribution of the frequency is highly consistent with the tracks of the strong cyclones entering the Arctic, suggesting a large contribution of the cyclones originating from the midlatitudes and the subarctic, in addition to the cyclones generated within the Arctic. Another area of relatively large frequency can be found over the Bering Sea, but this maximum is much lower than that on the North Atlantic side, indicating that strong winter cyclones over the Arctic have predominantly originated from the North Atlantic sector rather than the North Pacific.

When comparing the two time periods, we found a notable increase in the frequency of strong winter cyclones during recent decades, which has also mainly occurred over the North Atlantic Arctic (Fig. 3c). One maximum value of the increase in the frequency of strong winter cyclones appears to the southeast of Iceland, suggesting an eastward shift of the high frequency of strong cyclone occurrence from the earlier period to the later period (Fig. 3a vs. b). Another maximum value of the increase occurs over the area from the Barents Sea to the Kara-Laptev seas and adjacent coastal areas, extending into the central Arctic. This

indicates a recently increased count of strong cyclones propagating further north or a poleward shift of strong cyclone tracks. The changes in the high frequency of strong cyclone occurrence are consistent with the poleward shift of the polar center of action of the leading large-scale atmospheric circulation mode during recent decades, leading to a spatial pattern transition from the zonally oriented AO to a meridionally aligned Arctic Rapid change Pattern (ARP)[39], further suggesting interactive processes between synoptic and large-scale atmospheric circulations. The increase in strong cyclones over the central Arctic also agrees with recent studies that the enhanced cyclone activity has resulted in a collapse of the winter Beaufort High during recent winters[42–44].

During summer, the results generally demonstrate similar spatial patterns to those during winter over the North Atlantic Arctic (Fig. 3d, e). As during winter, the maximum frequency of strong summer cyclones occurs over the Irminger Sea and Iceland Basin. However, large seasonal differences can be clearly observed. One major difference is an overall lower frequency during summer than winter for both multidecadal time periods (Note the different color scales for winter and summer). The other major difference is the high frequency covering most of the Arctic Ocean with the second maximum center over the central Arctic during summer, which contrasts with the winter season when high frequencies are mainly limited to the North Atlantic side.

The comparison between the two multidecadal periods also shows a pronounced increase in the frequency of strong summer cyclone occurrence over the entire Arctic. The most prominent feature is the dramatic increase over the central Arctic Ocean, which is clearly illustrated in Fig. 3f. The maximum frequency and its increase during recent decades in the central Arctic Ocean are obviously not an extension of the high frequencies from the North Atlantic and Nordic Seas, suggesting that a substantial portion of the strong summer cyclones, in particular their increase since the mid-1980s, over the central Arctic Ocean have been mainly generated within the Arctic domain. This can also be clearly seen in the cyclone tracks, including cyclogenesis and cyclolysis locations, shown by Supplementary Fig. S3g–l in the three reanalysis datasets. Recall that the strong cyclones here are defined using their averaged central SLPs over the duration within the Arctic. Therefore, the variation of cyclone central SLPs, or intensities, during their propagation does not influence the frequency analyzed here.

Driving mechanisms of intensifying Arctic cyclone activity. To understand the causations of the intensification of Arctic cyclone activity, we examined the underlying physical mechanisms, including the baroclinic instability, the tropospheric jet streams and associated waves, and the stratospheric vortex. Because all three reanalysis datasets present highly consistent results and the ERA5 has the highest spatial resolutions, we elected to employ the ERA5 for the mechanistic analysis. We first analyzed baroclinic instability, which is the fundamental driver for cyclogenesis and development, based on the maximum Eady Growth Rate (EGR, see "Methods")[45].

We calculated EGR at the level of 900 hPa because baroclinic instability mainly occurs in the lower troposphere and near the surface in strong Arctic summer cyclones[16]. The spatial distributions of the high EGR for the two multidecadal periods are consistent with the cyclogenesis areas and cyclone tracks for both winter and summer (Supplementary Fig. S4)[1,2]. In the North American and North Atlantic sectors, the large EGR areas are located on the lee side of the Rocky Mountains, along the U.S. East Coast, and from the U.S. East Coast to the North Atlantic area along the path of the North Atlantic Current (NAC). In the Asian and North Pacific sector, the large EGR occurs to the north and east of the Tibetan Plateau, along the Asian east coast, and from Japan to the North Pacific Ocean following the Kuroshio Extension and North Pacific Current (KE-NPC). The high EGRs are attributable to either the topographic effects, strong surface thermal contrast, or surface diabatic heating. The Arctic region has lower EGR except over the Nordic Seas, where the North Atlantic warm water inflow meets the Arctic cold water and sea ice outflows. Generally, the EGR during summer is weaker than during winter, especially over the oceans.

When examining the changes in the climatological mean winter and summer EGR from the first to second multidecadal period, we found an increase in the winter EGR over broad areas from the midlatitudes to the Arctic during recent decades (Fig. 4a). An anomalously large increase has occurred over the North Atlantic Arctic from the Greenland Sea to Fram Strait and the northern Barents Sea. During recent decades, the poleward North Atlantic warm water inflow has been considerably enhanced according to observational data[39,46,47]. This enhancement has increased the open ocean-sea ice thermal contrast and reduced the atmospheric static stability, contributing to the increase in EGR. In addition, sea ice has substantially retreated[48], causing a poleward shift of the sea ice edge and, in turn, the area with a large increase in EGR, in particular in the northern Barents Sea. The enhanced EGR has supported the increase in cyclone

frequency over the same area (Fig. 3c). Another pronounced winter EGR increase has occurred along 50°N across much of the North Atlantic Ocean. The largely increased EGR over the mid and eastern North Atlantic Ocean suggests an eastward extension of the large baroclinic zone during recent decades (Fig. 4a, Supplementary Fig. S4a, b), which favors cyclogenesis and cyclone intensification there.

However, the winter EGR has decreased strongly over the northwestern North Pacific area near Japan and relatively weakly in a band across the subpolar North Atlantic from the Labrador Sea to the Irminger Sea and the Iceland Basin. The latter is the area where the North Atlantic "warming hole" has occurred[49,50]. The Norwegian Sea and the southern Barents Sea have also shown a decrease in EGR. By itself, the decreased EGR over these areas does not support the overlying increased cyclone frequency (Fig. 4a vs. Fig. 3c).

To resolve this discrepancy, we examined the large-scale atmospheric circulation in the troposphere and stratosphere. The winter 500 hPa GHT has shown a deepened and eastward shifted trough over the Labrador Sea and the southern tip of Greenland during recent decades (Fig. 4b and Supplementary Fig. S5a, b). Considering the increased 500 hPa GHT over the North Atlantic midlatitudes and the Mediterranean Sea, the changes in the circulation pattern have a strong projection on the positive AO/NAO phase over the North Atlantic sector. Overall, the AO index and the EnCAI are highly correlated at a monthly scale (with a correlation coefficient of 0.71) though the AO index has a much smaller increasing trend (Supplementary Fig. S1). This statistically reflects two-way interactions between the large-scale atmospheric circulation variability and synoptic-scale cyclones, as discussed earlier. Dynamically, the amplification of the jet stream waves (planetary Rossby waves propagating along the jet streams) associated with the deepened trough steers the cyclones generated over the North Atlantic, where EGR has increased, to propagate northeastward to the Nordic Seas and intensifies the cyclones during their propagation.

At the same time, the winter Planetary Stratospheric Polar Vortex (P-SPV) has also experienced dramatic changes, as depicted by the differences of 50 hPa GHT (Fig. 4c). An anomalous P-SPV center has occurred over Greenland during recent decades. To understand the impacts of P-SPV on the tropospheric circulation, we examined Potential Vorticity (PV) in the lower stratosphere and found an enhanced positive PV anomaly at 300 hPa over the area from the Labrador Sea to the Iceland Basin (Fig. 4d). The level of 300 hPa shows a climatological mean PV of 2.7 PVU over this area (Supplementary Fig. S6a, b), just above the dynamic tropopause (defined as the surface of 2.0 PVU[51]). The enhanced positive PV anomaly indicates a downward intrusion of the P-SPV into the climatological troposphere. Therefore, the changed P-SPV between 1986/86–2020/21 and 1950/51–1984/85 has further intensified the troposphere trough and jet stream waves and, in turn, surface cyclones, according to the stratospheric downward influence theory and PV dynamics[51,52]. Taken together, the changed tropospheric and stratospheric circulations have driven intensification and northeastward propagation of North Atlantic cyclones to increase the cyclone frequency over the subpolar North Atlantic, Norwegian Sea, and southern Barents Sea, where EGR has decreased during recent decades.

Note that the anomalous P-SPV center over Greenland is displaced from P-SPV's climatological mean location over the Eurasian Arctic Ocean (Supplementary Fig. S7a, b), consistent with the weakening of P-SPV during recent decades[53]. The weakened P-SPV could be attributed to destructive interference of the upward propagation of planetary waves excited by the amplified Arctic warming[54].
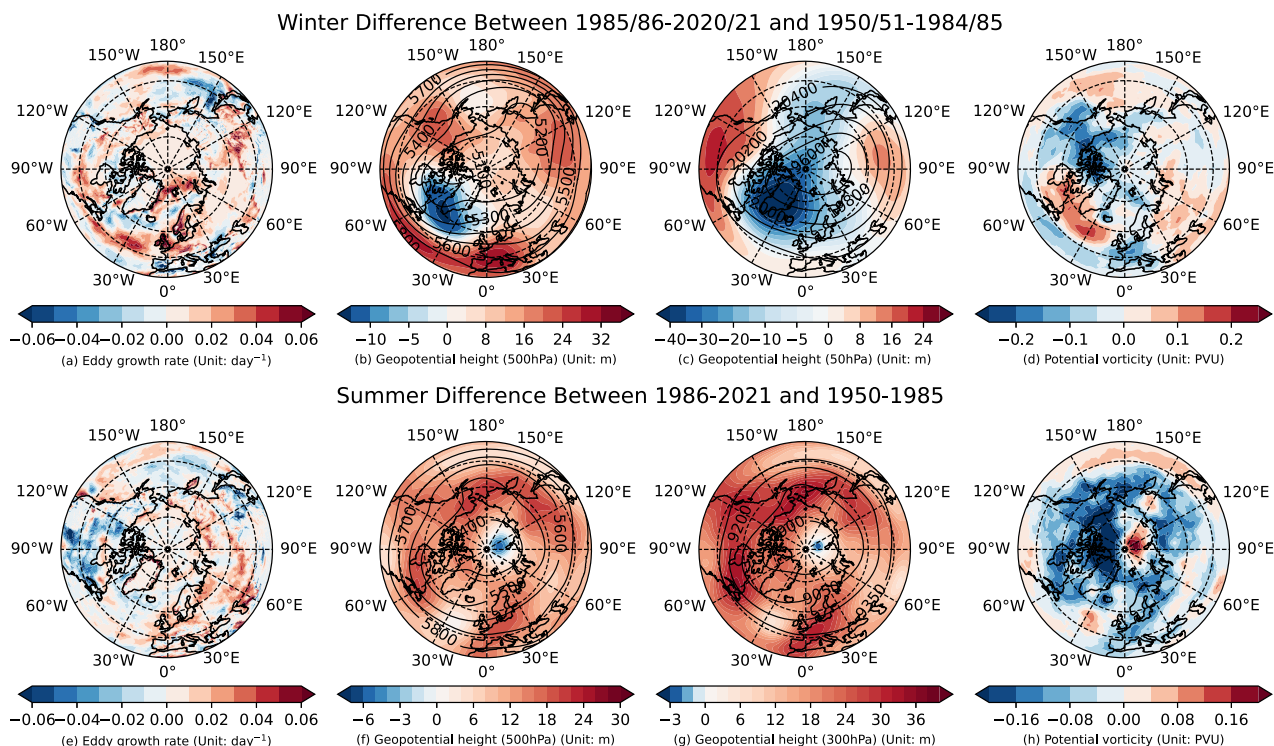
Fig. 4 Mechanisms driving increases in Arctic cyclone frequencies. Differences (color shading) of winter **a** maximum Eady growth rate (EGR) at 900 hPa, **b** geopotential height at 500 hPa, **c** geopotential height at 50 hPa, and **d** potential vorticity at 300 hPa between 1985/86–2020/21 and 1950/51–1984/85. The black contours in (**b**) and (**c**) are the climatological mean geopotential height at 500 hPa and 50 hPa, respectively, for the period of 1985/86–2020/21. **e**–**h** are the same as (**a**–**d**) but for summer between 1986–2021 and 1950–1985, except for (**g**) at 300 hPa.

During the summers of recent decades, the EGR has shown an increase over the Arctic and the Eurasian continent but a decrease over North America (Fig. 4e). The maximum increase has mainly occurred over the Eurasian Arctic shelf seas and the adjacent land areas, as well as the Beaufort Sea, supporting the increased cyclone frequency over the Eurasian side of the central Arctic (Fig. 3d–f). Previous studies show the largest summertime increase in meridional temperature gradient along the coastline[55]. However, the increase in the baroclinic instability, measured here by EGR, covered broader ocean and land areas, consistent with the spatial distribution of the increased frequency of strong cyclone occurrence.

As during winter, the baroclinic instability is also not the sole dynamic mechanism during summer. When comparing Figs. 3f and 4e, we found that the largest increase in the cyclone frequency does not occur in the area with the maximum increase in EGR. We therefore examined the large-scale atmospheric circulation and found that the 500 hPa GHT has substantially increased over most of the Northern Hemisphere during recent decades. However, a deepened, synoptic-scale low center has occurred over the Eurasian side of the central Arctic Ocean (Fig. 4f and Supplementary Fig. S5c, d). The widespread GHT increase could result from the surface and lower troposphere warming according to the Quasi-Geostrophic (QG) theory[56]. However, the deepened GHT low center, or the strengthened tropospheric vortex, over the central Arctic is evidently caused by the atmospheric dynamics, given the amplified Arctic warming.

Although the P-SPV only emerges during the winter season as an influence on the troposphere circulation, it has recently been found that synoptic-scale, axisymmetric vortices can occur in the Arctic lower stratosphere along with strong summer cyclones[15–17]. We therefore examined 300 hPa GHT, where the climatological mean PV values reached about 3.8 PVU over the

central Arctic during the two multidecadal periods (Fig. 3c, d). This level was also just above the tropopause, representing the lower stratosphere. When comparing the two time periods, we found a strengthened Synoptic, lower Stratospheric Arctic Vortex (S-SAV), vertically stacked above the tropospheric vortex over the Eurasian side of the central Arctic, during recent decades (Fig. 4f, g). Corresponding to the strengthened S-SAV, an enhanced synoptic scale, positive PV anomaly can be clearly identified at the same level (Fig. 4h), indicating that the dynamic tropopause has moved further down to below 300 hPa. Therefore, the S-SAV has intruded downward to the level of the climatological troposphere.

Arctic summer cyclone structure and dynamics are emerging, leading-edge research topics. A recent case study[16] of strong summer cyclone dynamics reveals that in association with the downward intrusion of S-SAV, a warm core develops from the upper troposphere to the lower stratosphere due to downward-motion-induced adiabatic heating. As a consequence, jet streams form following the thermal wind balance around the positive PV anomaly, or the downward intruded S-SAV, to spin up cyclonic circulation in the troposphere. Examination of the tropospheric and lower stratospheric circulation change (Fig. 4f–h) indicates that the enhanced PV anomaly, or the deepened downward intrusion of S-SAV, could therefore have strengthened the tropospheric vortex and, in turn, surface cyclones during recent decades. This mechanism provides an explanation for the maximum increase in the strong summer cyclone frequency over the central Arctic Ocean, where baroclinicity has only been moderately enhanced.

Note that although the increase in strong winter and summer cyclone frequencies has been caused by the changes in both baroclinic instability and atmospheric circulation, strong summer cyclones demonstrate dynamic structure and driving mechanisms
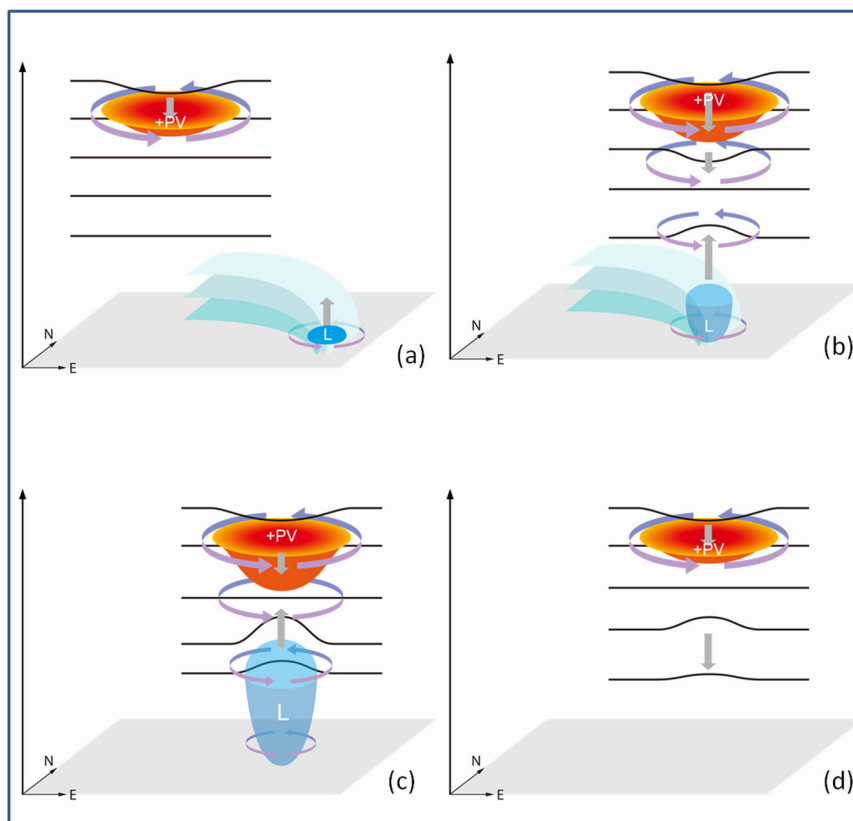
Fig. 5 Schematic diagram of intense summer cyclone development. a A baroclinic instability-driven cyclone is generated at the surface in the lower troposphere and, at the same time, a Synoptic, axisymmetric lower Stratospheric Arctic Vortex (S-SAV) occurs. A positive potential vorticity (+PV) anomaly emerges associated with S-SAV; **b** the cyclone and S-SAV move together to be vertically stacked so that both the surface-lower tropospheric baroclinic instability and the lower stratospheric +PV anomaly intensify the cyclone to maturity. Correspondingly, a lower-level cold core and an upper-level warm core structure form; **c** the surface-lower tropospheric baroclinicity weakens and disappears. The cyclone transforms to an equivalent barotropic structure with persisting lower-level cold and upper-level warm cores; the downward intrusion of the S-SAV and associated +PV anomaly maintain the cyclone over an extended period; and **d** the S-SAV weakens, and the cyclone dissipates. The horizontal black curves represent the contours of potential temperature. The horizontal and vertical arrows indicate the cyclonic circulation and vertical motions, respectively. The cyan and light cyan color surfaces show a baroclinic front associated with the cyclone. The light blue oval at the lower level indicate a cold core and the red bowl shape at the upper level show a warm core and +PV anomaly. (Reproduced based on refs. [16,17]).

distinct from strong winter cyclones as depicted in Fig. 4. More specifically, two predominant characteristics have been revealed in dynamic diagnoses and composite analyses of strong summer cyclones through their development (Fig. 5):[16,57] (1) a lower stratospheric warm core and tropospheric cold core structure; and (2) a transition from baroclinic to equivalent barotropic phase. The baroclinic instability mainly drives cyclogenesis and initial intensification. When the cyclone reaches its mature phase, its structure becomes equivalent barotropic. Then, the downward intrusion of the S-SAV plays a predominant role in intensifying cyclones and sustaining their intensity over an extended time period. The enhanced lower tropospheric baroclinic instability and strengthened tropospheric and lower stratospheric vortices identified during recent decades have intensified these dynamic processes, causing a long-term increase in the frequency of strong summer cyclones.

It is worth stressing again that the S-SAV (also named tropopause polar vortex in some recent studies[58]) fundamentally differs from the P-SPV. The former occurs during summer at synoptic scales in the lower stratosphere, demonstrating an axisymmetric structure and vertically stacked above the tropospheric vortex and surface cyclone over the central Arctic (Fig. 4f, g). The S-SAV intensifies surface cyclones through downward spin-up by PV anomaly-induced jet streams.

However, the P-SPV only emerges during winter in the subarctic and midlatitudes, with the strongest intensity in the upper stratosphere and an association with the planetary Rossby waves. The anomalous P-SPV center is vertically tilted from the tropospheric vortex and surface cyclones (Fig. 4b, c) and acts to intensify surface cyclones by enhancing baroclinicity[51,59–62].

Summary and discussion

We have detected robust, physically based intensification of Arctic cyclone activity by integrating multiple reanalysis datasets covering seven decades from the 1950s to 2021, substantially extending the time periods used in previous studies. In the analysis, we also employed an improved cyclone identification and tracking algorithm and an improved integrative metric portraying the overall Arctic cyclone activity. The results obtained here may help reconcile the different conclusions and debates that have recently emerged[11,27–36].

More specifically, a cyclone count and duration analysis as a function of cyclone intensity reveals a long-term shift of the maximum count from weaker to stronger cyclones and a pronounced lengthening of the duration of strong cyclones. The count of strong cyclones [the central SLP averaged over the duration within the Arctic deeper than 980 hPa (990 hPa) for winter (summer)] has increased by about 29.7% (35.3%) from 37

(34) each winter (summer) in the 1950s to 48 (46) each winter (summer) in the 2010s. This suggests that the intensification of Arctic cyclone activity has been predominantly attributable to the increased count and duration of strong cyclones. Further spatial structure analysis shows a large increase in the frequency of strong cyclone occurrence over the Arctic and a poleward shift of strong cyclone tracks toward the central Arctic Ocean during recent decades. Seasonality can also be clearly seen in the frequency increases. During winter, the maximum increase has occurred over the North Atlantic Arctic, which can be primarily attributed to the enhanced poleward propagation of strong cyclones originating in the midlatitudes and subarctic. However, the maximum increase during summer has appeared mainly over the central Arctic.

In the causation analysis, we found that the driving mechanisms for the intensification of Arctic cyclone activity have been ascribed to both enhanced lower tropospheric/surface baroclinic instability and the changed large-scale atmospheric circulation, including the stratosphere-troposphere interactions. Winter baroclinic instability has been largely enhanced along the NAC and the KE-NPC in the midlatitude oceans and over the marginal ice zone/along the ice edge in the Arctic during recent decades. Although there has been an enhancement of summer baroclinic instability over the marginal ice zone/along the ice edge in the Arctic, the maximum increase has occurred mainly over the Eurasian Arctic coastal areas. The highly impactful, anomalously intense summer cyclones of 2012 and 2016 originated in these areas[14,17,18], consistent with the enhanced baroclinic instability.

Changes in the large-scale atmospheric circulation have also played crucial roles in intensifying Arctic cyclone activity but with distinct dynamics between winter and summer. During winter, a deepened tropospheric trough and associated amplification of the planetary tropospheric jet stream waves have occurred across the subpolar North Atlantic from the Labrador Sea to the Irminger Sea and the Iceland Basin during recent decades. They have steered northeastward propagation of cyclones from the North Atlantic, where the enhanced baroclinic instability favored cyclogenesis and cyclone deepening, into the Arctic and intensified the cyclones during their propagation. At the same time, an anomalous P-SPV center and an associated strengthening of positive PV anomaly have occurred over the same area, intensifying the tropospheric trough and, in turn, the surface cyclones, according to the downward influence theory and PV dynamics[51].

It is worth mentioning that not only has the anomalous P-SPV center over Greenland intensified cyclones and steered cyclone tracks poleward, as analyzed in this study, but it has also played important roles in causing extreme cold events over North America[63,64]. This suggests systematic effects of large-scale atmospheric circulation changes on both the Arctic and midlatitudes. In addition, the North Atlantic "warming hole" has also increased the thermal contrast to its south and, in turn, contributed to the increase in North Atlantic EGR, showing the impacts of the long-term sea surface temperature changes on cyclone activity. The "warming hole" may be related to the changes in the Arctic Ocean freshwater export and Greenland Ice Sheet meltwater runoff into the subpolar North Atlantic Ocean and the variability of the Atlantic Meridional Overturning Circulation (AMOC)[49,50].

During summer, a strengthened synoptic-scale tropospheric vortex has occurred over the central Arctic during recent decades. This contrasts with the widespread increase in the tropospheric GHT over most of the Northern Hemisphere. At the same time, the downward intruding S-SAV and the associated enhanced PV anomaly are vertically stacked above the tropospheric vortex.

Taken together, the strengthened tropospheric and lower stratospheric vortices form an equivalent barotropic structure. Arctic summer cyclone structures and dynamics represent an emerging research area. As recently revealed in a dynamical diagnosis[16] and supported by a composite analysis[57], strong summer cyclones exhibit distinct dynamic and thermodynamic structures and mechanisms from conventional midlatitude and subarctic cyclones. After their transition from initial baroclinically driven generation and intensification to an equivalent barotropic phase, the downward intrusion of the S-SAV plays a decisive role in spinning up the tropospheric vortex and, in turn, intensifying surface cyclones. The strengthened, downward intruded S-SAV during recent decades, as found in this study, enhances these processes. As a consequence, the changed S-SAV has intensified Arctic cyclone activity. It is worth stressing that although the stratospheric dynamics have played an important role in the Arctic tropospheric circulation variations and surface cyclone development during both winter and summer, their dynamic structures and processes are essentially different in the two seasons.

In addition, recent studies have also found an enhanced atmospheric moisture transport into the Arctic both by meridionally transformed large-scale atmospheric circulation and by cyclones propagating into the Arctic[7,9]. The precipitation is also projected to increase in the Arctic under the future greenhouse-gas emissions forcing scenarios[65,66]. The latent heat release associated with the increased tropospheric water vapor and precipitation would contribute to a further intensification of cyclone activity.

In this study, we employed only one cyclone identification and tracking algorithm. This improved algorithm can be universally applied to reanalysis datasets and model simulations with different spatial resolutions without a revision/adjustment of the cyclone criteria. Therefore, the cyclones in different reanalysis datasets are derived under the same standard, reducing the impacts of data uncertainties and potential influences of different algorithms. Nevertheless, a comparison of 10 other algorithms applied to the ERA-interim reanalysis shows considerable differences in the detected cyclone central SLPs, although the cyclone locations showed good consistency[67]. Also, to overcome the challenges raised by higher spatial resolution reanalysis datasets such as ERA5, some studies remapped the native higher resolution to a lower resolution of the data for cyclone identification and tracking[68], which may add additional uncertainties on cyclone intensity and locations. To estimate the uncertainties caused by the algorithms, especially with higher resolution datasets, and to further improve the robustness of the detected changes in Arctic cyclone activity, a comparison of our newly improved algorithm with other algorithms is a priority for follow-up work.

The main findings of this study have important implications. Arctic cyclones drive poleward transient atmospheric heat and moisture transport, surface turbulent fluxes, and cloud formation, linking the Arctic with global climate and influencing the Arctic energy and water cycle. They are also a primary mechanism causing Arctic climate and weather extremes, which have dramatic socioeconomic and environmental impacts and can enhance atmosphere-sea ice-ocean interactions that cumulatively accelerate Arctic climate change. The study also contributes to an improved understanding of the highly debated Arctic-midlatitude linkages. The enhanced baroclinicity over the Northern Hemisphere revealed here, especially during winter, indicates that the changes in the atmospheric circulation are more complicated than what has been hypothesized based on the Arctic-amplification-induced decrease in the mean meridional temperature gradients[69]. Furthermore, although our study indicates

an intensification of Arctic cyclone activity along with global and Arctic warming, Arctic cyclone activity in the projected future warming climate highly depends on the changes in the near-surface baroclinicity and atmospheric dynamics. The former can be influenced by sea ice/ocean surface energy budgets and poleward ocean heat transport. The latter includes changes in the tropospheric jet streams and associated waves, as well as the stratospheric vortex. All of these could be comprehensively evaluated using the multimodal simulations and projections coordinated by the Coupled Model Intercomparison Project Phase 6 and/or the forthcoming Phase 7 (CMIP6 and 7). An Arctic cyclone intercomparison project based on the CMIP models could shed light on the large uncertainties inherent in the CMIP model projections of future changes in Arctic cyclone activity (cf. Fig. 4.29 of the Intergovernmental Panel on Climate Change's most recent assessment report[70]).

Methods

Reanalysis datasets. The data include six-hourly sea level pressures (SLPs), upper air geopotential heights (GHTs), temperatures, and winds in the Northern Hemisphere (north of 30°N) from three different reanalysis datasets: (1) the National Centers for Environmental Prediction-National Center for Atmospheric Research (NCEP-NCAR) reanalysis[71], (2) the fifth generation of the European Centre for Medium-Range Weather Forecasts (ECMWF) atmospheric reanalysis (ERA5)[72], and (3) the Japanese 55-year Reanalysis (JRA-55)[73,74]. The three reanalyses are available from the 1950s to present at spatial resolutions of 2.5° × 2.5°, 0.25° × 0.25°, and 1.25° × 1.25°, respectively.

Cyclone identification and tracking algorithm. The cyclone identification and tracking algorithm is an improved version based on our previous study[2]. The algorithm combines the requirement of an SLP minimum with other thresholds characterizing fundamental features of extratropical and Arctic cyclones, including minimum SLP gradient, isobar closure, maximum propagation distance, minimum lifetime, and selection of a primary cyclone center when multiple centers appear within one cyclone system. The major improvement in the new version is the calculation of the mean SLP gradients within a defined radius of candidate cyclone centers, instead of using two circles of adjacent grid points. The new version is therefore universally applicable to datasets at different resolutions without any adjustment of the resolution-dependent thresholds. In this study, we chose a radius of 350 km, assuring appropriate data sampling size to calculate the mean SLP gradients from the coarse resolution NCEP-NCAR reanalysis (2.5° × 2.5°; ~138.678 km × 277.371 km at 60°N) to the higher-resolution ERA5 (0.25° × 0.25°; ~13.869 km × 27.737 km at 60°N). The improved approach also makes it possible to capture large-size mesoscale cyclones, such as polar lows with spatial scales of 200 to 1000 km[75], which is within the resolution capabilities of ERA5.

Energy-based cyclone activity index (EnCAI). We introduced an improved integrative metric to measure the overall cyclone activity. In our previous study[2], we defined a cyclone activity index (CAI), which is the monthly mean of summed differences of cyclone central SLPs from the monthly climatological SLPs at the corresponding grid points through all time steps. Because cyclones may have similar central SLPs but different strength of winds, the improved metric includes new information on mean geostrophic winds derived from the mean SLP gradients in the improved index. We used an energy framework and hydrostatic approximation to define an energy-based cyclone activity index

(EnCAI; unit: Joule per unit mass, m² s⁻²):

$$\text{EnCAI} = \frac{1}{N_t} \sum_{n_t} \sum_{n} \left[-\frac{\Delta_v P}{\rho} + 0.5 \times \left(-\frac{1}{f\rho} \frac{\Delta_h P}{\Delta r} \right)^2 \right] \quad (1)$$

where P is SLP; $\Delta_v P$ the difference of cyclone central SLP from the monthly climatological SLP at the corresponding grid points; $\frac{\Delta_h P}{\Delta r}$ the mean horizontal SLP gradient; r the natural coordinate toward cyclone center; ρ the air density, using 1.225 kg m⁻³; and f the Coriolis parameter; n the number of cyclone centers at each time step; n_t the time step; and N_t the total number of time steps in each month. The first term on the right-hand side in Eq. (1) represents the potential energy, and the second term is the geostrophic kinetic energy. As with the original CAI, EnCAI also aggregates information on cyclone count, intensity, and duration for each month. The intensity in EnCAI is a measure of both how deep the cyclone central SLPs are relative to the monthly climatological SLP and how strong the winds are within cyclones.

Maximum Eady growth rate (EGR). The maximum Eady growth rate (EGR) is defined as:[51]

$$\text{EGR} = 0.3098 \frac{|f| \left| \frac{\partial \vec{v}}{\partial z} \right|}{N} \quad (2)$$

where f is the planetary vorticity, z the vertical coordinate, $\vec{v}$ the wind vector, N the Brunt-Vaisala frequency ($N^2 = \frac{g}{\theta} \frac{\partial \theta}{\partial z}$, g is the gravitational constant, and θ the potential temperature). In the calculation of EGR at 900 hPa, we used $\vec{v}$ and θ at three vertical levels 925, 900, and 875 hPa.

References

1. Hoskins, B. J. & Hodges, K. I. New perspectives on the Northern Hemisphere winter storm tracks. *J. Atmos. Sci.* **59**, 1041–1061 (2002).
2. Zhang, X., Walsh, J. E., Zhang, J., Bhatt, U. S. & Ikeda, M. Climatology and interannual variability of Arctic cyclone activity: 1948–2002. *J. Clim.* **17**, 2300–2317 (2004).
3. Bengtsson, L., Hodges, K. I. & Roeckner, E. Storm tracks and climate change. *J. Clim.* **19**, 3518–3543 (2006).
4. Serreze, M. C. & A. P. Barrett, A. P. The summer cyclone maximum over the central Arctic Ocean. *J. Clim.* **21**, 1048–1065 (2008).
5. Sorteberg, A. & Walsh, J. E. Seasonal cyclone variability at 70°N and its impact on moisture transport into the Arctic. *Tellus A* **60**, 570–586 (2008).
6. Bengtsson, L., Hodges, K., Koumoutsaris, S., Zahn, M. & Keenlyside, N. On the atmospheric water cycle of the polar regions. *Tellus A* **63**, 907–920 (2011).
7. Zhang, X. et al. Enhanced poleward moisture transport and amplified northern high-latitude wetting trend. *Nat. Clim. Change* **3**, 47–51 (2013).

8. Vihma, T. et al. The atmospheric role in the Arctic water cycle: a review on processes, past and future changes, and their impacts. *J. Geophys. Res. Biogeosci.* **121**, 586–620 (2016).

9. Villamil-Otero, G. A., Zhang, J., He, J. & X. Zhang, X. Role of extratropical cyclones in the recently observed increase in poleward moisture transport into the Arctic Ocean. *Adv. Atmos. Sci.* **35**, 85–94 (2018).

10. Simmonds, I. & Keay, K. Extraordinary September Arctic sea ice reductions and their relationships with storm behavior over 1979–2008. *Geophys. Res. Lett.* **36**, L19715 (2009).

11. Rinke, A. et al. Extreme cyclone events in the Arctic: wintertime variability and trends. *Environ. Res. Lett.* **12**, 094006 (2017).

12. Semenov, A., Zhang, X., Rinke, A., Dorn, W. & Dethloff, K. Arctic intense summer storms and their impacts on sea ice—a regional climate modeling study. *Atmosphere* **10**, 218 (2019).

13. Wei, J., Zhang, X. & Wang, Z. Impacts of extratropical storm tracks on Arctic sea ice export through Fram Strait. *Clim. Dyn.* **52**, 2235–2246 (2019).

14. Simmonds, I. & Rudeva, I. The great Arctic cyclone of August 2012. *Geophys. Res. Lett.* **39**, L23709 (2012).

15. Aizawa, T. & Tanaka, H. L. Axisymmetric structure of the long-lasting summer Arctic cyclones. *Polar Sci.* **10**, 192–198 (2016).

16. Tao, W., Zhang, J. & Zhang, X. The role of stratosphere vortex downward intrusion in a long-lasting late-summer Arctic storm. *Q. J. R. Meteorol. Soc.* **143**, 1953–1966 (2017).

17. Tao, W., Zhang, J., Fu, Y. & Zhang, X. Driving roles of tropospheric and stratospheric thermal anomalies in intensification and persistence of the Arctic Superstorm in 2012. *Geophys. Res. Lett.* **44**, 10017–10025 (2017).

18. Peng, L. et al. Role of intense Arctic storm in accelerating summer sea ice melt: an in-situ observational study. *Geophys. Res. Lett.* **48**, e2021GL092714 (2021).

19. Parkinson, C. L. & Comiso, J. C. On the 2012 record low Arctic sea ice cover: combined impact of preconditioning and an August storm. *Geophys. Res. Lett.* **40**, 1356–1361 (2013).

20. Dacre, H. F., Clark, P. A., Martinez-Alvarado, O., Stringer, M. A. & Lavers, D. A. How do atmospheric rivers form? *Bull. Am. Meteorol. Soc.* **96**, 1243–1255 (2015).

21. Boisvert, L. N., Petty, A. A. & Stroeve, J. C. The impact of the extreme winter 2015/16 Arctic cyclone on the Barents–Kara Seas. *Mon. Weather Rev.* **144**, 4279–4287 (2016).

22. Moore, G. W. K. The December 2015 North Pole warming event and the increasing occurrence of such events. *Sci. Rep.* **6**, 39084 (2016).

23. Kim, B.-M. et al. Major cause of unprecedented Arctic warming in January 2016: critical role of an Atlantic windstorm. *Sci. Rep.* **7**, 40051 (2017).

24. Graham, R. M. et al. Winter storms accelerate the demise of sea ice in the Atlantic sector of the Arctic Ocean. *Sci. Rep.* **9**, 9222 (2019).

25. Mattingly, K. S. et al. Strong summer atmospheric rivers trigger Greenland Ice Sheet melt through spatially varying surface energy balance and cloud regimes. *J. Clim.* **33**, 6809–6832 (2020).

26. Viceto, C. et al. Atmospheric rivers and associated precipitation patterns during the ACLOUD and PASCAL campaigns near Svalbard (May–June 2017): case studies using observations, reanalyses, and a regional climate model. *Atmos. Chem. Phys.* **22**, 1680–7324 (2022).

27. Simmonds, I., Craig, B. & Keay, K. Arctic climate change as manifest in cyclone behavior. *J. Clim.* **21**, 5777–5796 (2008).

28. Sepp, M. & Jaagus, J. Changes in the activity and tracks of Arctic cyclones. *Clim. Change* **105**, 577–595 (2011).

29. Tilinina, N., Gulev, S. K. & Bromwich, D. H. New view of Arctic cyclone activity from the Arctic system reanalysis. *Geophys. Res. Lett.* **41**, 1766–1772 (2014).

30. Zahn, M., Akperov, M., Rinke, A., Feser, F. & Mokhov, I. I. Trends of cyclone characteristics in the Arctic and their patterns from different reanalysis data. *J. Geophys. Res. Atmos.* **123**, 2737–2751 (2018).

31. Wickström, S., Jonassen, M. O., Vihma, T. & Uotila, P. Trends in cyclones in the high latitude North Atlantic during 1979–2016. *Q. J. R. Meteorol. Soc.* **146**, 762–769 (2019).

32. Valkonen, E., Cassano, J. & Cassano, E. Arctic cyclones and their interactions with the declining sea ice: a recent climatology. *J. Geophys. Res. Atmos.* **125**, 22021JD034366 (2021).

33. Orsolini, Y. J. & Sorteberg, A. Projected changes in Eurasian and Arctic summer cyclones under global warming in the Bergen Climate Model. *Atmos. Ocean. Sci. Lett.* **2**, 62–67 (2009).

34. Vavrus, S. J. Extreme Arctic cyclones in CMIP5 historical simulations. *Geophys. Res. Lett.* **40**, 6208–6212 (2013).

35. Akperov, M. et al. Cyclones and their possible changes in the Arctic by the end of the twenty first century from regional climate model simulations. *Theor. Appl. Climatol.* **122**, 85–96 (2015).

36. Day, J. J., Holland, M. M. & Hodges, K. I. Seasonal differences in the response of Arctic cyclones to climate change in CESM1. *Clim. Dyn.* **50**, 3885–3903 (2018).

37. Thompson, D. W. J. & Wallace, J. M. The Arctic Oscillation signature in wintertime geopotential height and temperature fields. *Geophys. Res. Lett.* **25**, 1297–1300 (1998).

38. Overland, J. E. & Wang, M. The Arctic climate paradox: the recent decrease of the Arctic Oscillation. *Geophys. Res. Lett.* **32**, L06701 (2005).

39. Zhang, X., Sorteberg, A., Zhang, J., Gerdes, R. & Comiso, J. C. Recent radical shifts in atmospheric circulations and rapid changes in Arctic climate system. *Geophys. Res. Lett.* **35**, L22701 (2008).

40. Jung, T., Vitart, F., Ferranti, L. & Morcrette, J.-J. Origin and predictability of the extreme negative NAO winter of 2009/10. *Geophys. Res. Lett.* **38**, L07701 (2011).

41. Santer, B. D. et al. Statistical significance of trends and trend differences in layer-average atmospheric temperature time series. *J. Geophys. Res. Atmos.* **105**, 7337–7356 (2000).

42. Moore, G. W. K., Schweiger, A., Zhang, J. & Steele, M. Collapse of the 2017 winter Beaufort High: a response to thinning sea ice? *Geophys. Res. Lett.* **45**, 2860–2869 (2018).

43. Ballinger, T. J. et al. Unusual west Arctic storm activity during winter 2020: another collapse of the Beaufort High? *Geophys. Res. Lett* **48**, e2021GL092518 (2021).

44. Moore, G. W. K. et al. Thick and old sea ice in the Beaufort Sea during summer 2020/21 was associated with enhanced transport. *Commun. Earth Environ.* **3**, 198 (2022).

45. Hoskins, B. J. & Valdes, P. J. On the existence of storm-tracks. *J. Atmos. Sci.* **47**, 1854–1864 (1990).

46. Polyakov, I. V. et al. One more step toward a warmer Arctic. *Geophys. Res. Lett.* **32**, L17605 (2005).

47. Smedsrud, L. H. et al. Nordic Seas heat loss, Atlantic inflow, and Arctic sea ice cover over the last century. *Rev. Geophys.* **60**, e2020RG000725 (2022).

48. Parkinson, C. L. Arctic sea ice coverage from 43 years of satellite passive-microwave observations. *Front. Remote Sens.* **3**, 1021781 (2022).

49. Gervais, M., Shaman, J. & Kushnir, Y. Mechanisms governing the development of the North Atlantic warming hole in the CESM-LE future climate simulations. *J. Clim.* **31**, 5927–5946 (2018).

50. Keil, P. et al. Multiple drivers of the North Atlantic warming hole. *Nat. Clim. Change* **10**, 667–671 (2020).

51. Hoskins, B. J., Mcintyre, M. E. & Robertson, A. W. On the use and significance of isentropic potential vorticity maps. *Q. J. R. Meteorol. Soc.* **111**, 877–946 (1985).

52. Haynes, P. Stratospheric dynamics. *Ann. Rev. Fluid Mech.* **37**, 263–293 (2005).

53. Seviour, W. J. M. Weakening and shift of the Arctic stratospheric polar vortex: internal variability or forced response? *Geophys. Res. Lett.* **44**, 3365–3373 (2017).

54. Kim, B.-M. et al. Weakening of the stratospheric polar vortex by Arctic sea-ice loss. *Nat. Commun.* **5**, 4646 (2014).

55. Day, J. J. & Hodges, K. I. Growing land-sea temperature contrast and the intensification of Arctic cyclones. *Geophys. Res. Lett.* **45**, 3673–3681 (2018).

56. Bluestein, H. B. *Synoptic-Dynamic Meteorology in Midlatitudes, Observations and Theory of Weather Systems*, Vol. 2, 594 (Oxford University Press, 1993).

57. Vessey, A. F., Hodges, K. I., Shaffrey, L. C. & Day, J. J. The composite development and structure of intense synoptic-scale Arctic cyclones. *Weather Clim. Dyn.* **3**, 1097–1112 (2022).

58. Bray, M. & Cavallo, S. M. (2022), Characteristics of long-term tropopause polar vortices. *Weather Clim. Dyn.* **3**, 251–278 (2022).

59. Davis, C. A. & Emanuel, K. A. Potential vorticity diagnostics of cyclogenesis. *Mon. Weather Rev.* **119**, 1929–1953 (1991).

60. Hirschberg, P. A. & Fritsch, J. M. Tropopause undulations and the development of extratropical cyclones. Part II: Diagnostic analysis and conceptual model. *Mon. Weather Rev.* **119**, 518–550 (1991).

61. Hakim, G. J., Keyser, D. & Bosart, L. F. The Ohio Valley wave-merger cyclogenesis event of 25–26 January 1978. Part II: Diagnosis using quasigeostrophic potential vorticity inversion. *Mon. Weather Rev.* **124**, 2176–2205 (1996).

62. Rossa, A. M., Wernli, H. & Davies, H. C. Growth and decay of an extra-tropical cyclone's PV-tower. *Meteorol. Atmos. Phys.* **73**, 139–156 (2000).

63. Overland, J. et al. How does the Arctic influence midlatitude winter extreme weather events? *Environ. Res. Lett.* **16**, 043002 (2021).

64. Zhang, X. et al. Extreme cold events from East Asia to North America in Winter 2020/21: comparisons, causes, and future implications. *Adv. Atmos. Sci.* **39**, 553–565 (2022).

65. Bintanja, R. & Selten, F. Future increases in Arctic precipitation linked to local evaporation and sea-ice retreat. *Nature* **509**, 479–482 (2014).

66. McCrystall, M. R. et al. New climate models reveal faster and larger increases in Arctic precipitation than previously projected. *Nat. Commun.* **12**, 6765 (2021).

67. Simmonds, I. & Rudeva, I. A comparison of tracking methods for extreme cyclones in the Arctic basin. *Tellus A Dyn. Meteorol. Oceanogr.* **66**, 25252 (2014).

68. Crawford, A. D. & Serreze, M. C. Does the summer Arctic frontal zone influence Arctic Ocean cyclone activity? *J. Clim.* **29**, 4977–4993 (2016).

69. Francis, J. A. & Vavrus, S. J. Evidence linking Arctic amplification to extreme weather in mid-latitudes. *Geophys. Res. Lett.* **39**, L06801 (2012).

70. IPCC. *Technical Summary of Climate Change 2021: The Physical Science Basis.* Contribution of Working Group I to the Sixth Assessment Report of the Intergovernmental Panel on Climate Change. https://doi.org/10.1017/9781009157896.002 (Cambridge University Press, 2021).

71. Kalnay, E. et al. The NCEP/NCAR 40-year reanalysis project. *Bull. Am. Meteorol. Soc.* **77**, 437–472 (1996).

72. Hersbach, H. et al. The ERA5 global reanalysis. *Q. J. R. Meteorol. Soc.* **146**, 1999–2049 (2020).

73. Kobayashi, S. et al. The JRA-55 reanalysis: general specifications and basic characteristics. *J. Meteorol. Soc. Jpn* **93**, 5–48 (2015).

74. Harada, Y. et al. The JRA-55 reanalysis: representation of atmospheric circulation and climate variability. *J. Meteorol. Soc. Jpn* **94**, 269–302 (2016).

75. Stoll, P. J. A global climatology of polar lows investigated for local differences and wind-shear environments. *Weather Clim. Dyn.* **3**, 483–504 (2022).

76. Zhang, X. et al. Arctic cyclones have become more intense and longer-lived over the past seven decades. figshare https://doi.org/10.6084/m9.figshare.23574855 (2023).

Acknowledgements

Author contributions

X.Z. led the study, improved the cyclone tracking algorithm and computed cyclone data, and wrote the paper. H.T. computed EGR, climatological geopotential height, and PV and plotted figures, J.Z. also plotted figures, H.T., J.Z., J.E.W., E.L.R., B.H., T.J.B., and W.W. contributed to result discussions and the paper writing.

Competing interests

The authors declare no competing interests.

Additional information

Supplementary information The online version contains supplementary material available at https://doi.org/10.1038/s43247-023-01003-0.

Correspondence and requests for materials should be addressed to Xiangdong Zhang.

Peer review information *Communications Earth & Environment* thanks G.W.K. Moore and the other anonymous reviewer(s) for their contribution to the peer review of this work. Primary handling editors: Sylvia Sullivan, Heike Langenberg. A peer review file is available.

Reprints and permission information is available at http://www.nature.com/reprints

Publisher's note Springer Nature remains neutral with regard to jurisdictional claims in published maps and institutional affiliations.